

The Effect of Motion-Induced Eddy Currents on Three-Axis MFL Signals for High-Speed Rail Inspection

Guanyu Piao^{ID}, Jiaoyang Li^{ID}, Lalita Udupa, Satish Udupa, *Life Fellow, IEEE*, and Yiming Deng^{ID}

Department of Electrical and Computer Engineering, Michigan State University, East Lansing, MI 48824 USA

Nondestructive testing (NDT) methods are widely used in the rail industry to detect rolling contact damage (RCD) defects to ensure railway safety. With the need of monitoring millions of miles of rail tracks more effectively and efficiently that leads to improved rail safety, reliability, and optimized assets management, the research on high-speed and high-accuracy NDT methods that can obtain high signal-to-noise ratio (SNR) and high sensitivity defect signals at higher speeds is of vital importance. Magnetic flux leakage (MFL) is one of the NDT methods used for high-speed rail inspection, which is suitable for detecting surface and subsurface RCD defects on railhead, but the measured MFL signals are distorted severely by the effect of motion-induced eddy currents (MIEC). However, the fundamental understanding of the mechanism of MIEC generation, distribution, and magnitude is lacking, and the physical interaction between MIEC and MFL measurement during high-speed rail inspection has not been well studied. This article investigates the effect of MIEC on three-axis MFL signals through 3-D finite-element method (FEM) simulations. The 3-D distributions of MIEC and 2-D image signals of MFL measurements for high-speed rail MFL inspection are presented and analyzed. The simulations are conducted with an inspection speed range of 0–62.5 mi/h, and a surface hemisphere-type defect and subsurface hole-type defect are both considered. The results show that the motion between the magnetizer and the rail will generate two types of MIEC, which in turn decreases the peak values of three-axis MFL signals from the subsurface defect and affects the MFL signals spatially, especially the base values along rail transverse and vertical directions. The effect of MIEC on the three-axis MFL signals in terms of SNR, sensitivity, and asymmetry is discussed.

Index Terms—3-D numerical simulations, high-speed rail inspection, magnetic flux leakage (MFL), motion-induced eddy current (MIEC), rolling contact damage (RCD).

I. INTRODUCTION

RAILWAY transportation has become one of the main modes of transferring people and goods in modern society. Nowadays, there are more than 800 000 mi railways around 140 countries that connect our world, of which the United States operates more than 156 000 mi of railways, ranking first in the world [1]. Unfortunately, railway accidents that happened in recent years show that railway transportation still faces huge safety challenges. In Europe, 18746 railway accidents were reported between 2010 and 2019 [2], whereas in China, more than 10 000 fatalities were reported in railway accidents over the past decade [3]. In the United States, an average of 2000 railway accidents is happening each year, causing about \$300 million in economic losses, 70% of which are caused by severe derailments [4]. Rail defects evolved from rolling contact damage (RCD) are one of the main causes of derailments [5], [6]. The initiation of RCD and its propagation mechanism are governed by the contact stresses, traction forces on rails along with shear stresses and residual stresses, which continually gets more severe with higher train speed, more frequent usage, and increased loads. Thus, regular inspection and maintenance of rail RCD defects through efficient and accurate techniques are essential to railway safety.

Nondestructive testing (NDT) methods are widely used for rail defect inspection, including ultrasonic testing (UT),

electro-magnetic acoustic transducer (EMAT), magnetic flux leakage (MFL), eddy current testing (ECT), vision inspection system (VIS), electromagnetic field imaging (EMFI), and so on [7]. UT methods perform well in detecting deep internal defects of rail tracks due to the good penetration capability of ultrasonic waves; however, UT methods are inadequate to detect and characterize surface initiated RCD defects due to the ultrasonic near-surface resolution issues [8]–[10]. Furthermore, clusters of smaller surface cracks, spalling, shelling, and flaking inhibit UT beams from penetrating inside and prevent reliable inspection of the underlying material. Comparing to UT methods, EMAT methods do not require a couplant and have the capability of detecting surface and deep internal defects simultaneously; however, the inspection speed of EMAT methods is much lower than other NDT methods [11], [12]. MFL methods are suitable for detecting surface and subsurface railhead defects and usually utilize Hall-effect sensors or coil sensors to obtain three-axis MFL signals near defects. In high-speed rail inspection, due to the effect of motion-induced eddy currents (MIEC), the measured MFL signals are seriously distorted [13], [14]. ECT methods are usually used to detect small cracks on the surface or near surface of railhead with high sensitivity; however, the variation of liftoff values will introduce severe interference to the measured ECT signals during high-speed inspection [7], [15], [16], causing a low signal-to-noise ratio (SNR). VIS methods have the unique advantage of detecting surface RCD defects with high speed and high resolution; however, they cannot detect subsurface and internal deep defects [17]. In [18], the use of EMFI method for RCD defect characterization was presented, especially the quantification of the RCD severity and

Manuscript received November 3, 2020; revised January 2, 2021; accepted February 10, 2021. Date of publication February 19, 2021; date of current version March 18, 2021. Corresponding author: Y. Deng (e-mail: dengyimi@egr.msu.edu).

Color versions of one or more figures in this article are available at <https://doi.org/10.1109/TMAG.2021.3060390>.

Digital Object Identifier 10.1109/TMAG.2021.3060390

0018-9464 © 2021 IEEE. Personal use is permitted, but republication/redistribution requires IEEE permission.
See <https://www.ieee.org/publications/rights/index.html> for more information.

TABLE I
NDT METHODS AND EQUIPMENT IN RAIL INDUSTRY

Method	Equipment	Highest Speed	Deficiency
UT	Portable devices, vehicles, trains	50 mph	Low accuracy for surface defects [7–10]
EMAT	Vehicles	6 mph	Low inspection speed [11,12]
MFL	Vehicles, trains	45 mph	Effect of MIEC [13,14]
ECT	Portable devices, vehicles, trains	45 mph	Skin-depth effect, variation of lift-off values [7,15,16]
VIS	Trains	200 mph	Cannot assess subsurface and internal defects [17]

surface-breaking crack depth measurement, and the study of liftoff values was also conducted to understand the effect of an air gap on detection and characterization performance.

In practice, the sensors utilizing the aforementioned NDT methods are installed in three types of rail inspection systems, including manually operated portable devices, hi-rail vehicles, and rail inspection trains [7], [19], [20]. Generally, the speed ranges of portable devices, hi-rail vehicles, and inspection trains are 0–5, 5–25, and 50–200 mi/h (or mph), respectively. Table I shows a summary of the NDT methods and inspection systems applied in the rail industry [7]–[20]. Nowadays, with the need for monitoring millions of miles of rail tracks more effectively and efficiently that leads to improved rail safety, reliability, and optimized assets management, one of the great challenges is to develop high-speed and high-accuracy NDT methods that can obtain high SNR, high sensitivity, and specificity defect signals at the speed of up to 60 mi/h. However, each NDT method has its own limited detection capability for different types of rail defects and is affected by high-speed negative effects due to short sensor response time, liftoff variation, and MIEC effect, causing low sampling rate, low detection accuracy, and low SNR. Therefore, the research on investigating and mitigating the high-speed negative effects on the NDT methods is very important and attracts more attention.

This article focuses on the high-speed effect on the MFL method in terms of mechanism analyses and simulation studies to reveal the physical interaction between the source of the effect and the MFL measurement. Some existing works have been carried out for the high-speed effect on the MFL inspection [13], [14], [21]–[27]. In [13] and [21], 2-D simulations based on the finite-element method (FEM) were developed for high-speed inspection of surface RCD defects, where the inspection speed was from 0 to 67.5 mi/h. The results showed that the shape and magnitude of MFL signals were distorted due to the effect of MIEC, resulting in lower SNR as the inspection speed increased. In [22]–[24], 3-D FEM simulations were presented for the high-speed MFL method on the oil and gas pipeline inspection, and the distribution of MIEC and the distortion of three-axis MFL signals were analyzed. The study of utilizing the generation of MIEC as a way of detecting defects was also considered [25], [26]. In [25], subsurface defects can be detected and evaluated by using the diffusion of MIEC, whereas in [26], a rotating magnet array-based MIEC thermography method was proposed to increase the intensity of MIEC with higher scanning speed

to benefit the defect detection. In [27], it is found that the MIEC effect is not the only factor to influence MFL signals, and the effect of dynamic magnetization and magnetic hysteresis is considered as the main factor that alters the intensity and distribution of MFL signals for the high-speed MFL inspection. Meanwhile, a specially designed high-speed experimental platform was employed to verify the dynamic magnetization effect and probability of a high-speed MFL test. Recently, Antipov and Markov [14] presented the 3-D FEM simulation results on high-speed rail MFL inspection for subsurface hole-type defects, and the simulation results were verified by the obtained experimental results. The distribution of magnetic fields along the horizontal and transverse sections of rail tracks was presented and discussed. The simulation and experimental results both showed that the peak-to-peak values of MFL signals decreased when the speed increased from 20 to 50 mi/h. In addition, the optimal magnetic polar distance and the sensor measuring position were also discussed.

However, the fundamental understanding of the mechanism of MIEC generation, distribution, and magnitude is lacking, and the physical interaction between MIEC and MFL measurement during high-speed rail inspection has not been well studied. To address this issue, this article investigates the effect of MIEC on three-axis MFL signals in depth through mechanism analysis and 3-D FEM simulation modeling. The 3-D distributions of MIEC and the 2-D image signals of MFL measurements for high-speed inspection are presented and analyzed. The main contribution of this article is focused on the MIEC distributions, including two types of MIEC, and how the MIEC distributions will affect the magnetic field distributions as well as three-axis 2-D MFL signals at different speeds. The simulations are conducted at an inspection speed range of 0–62.5 mi/h. Meanwhile, in practice, RCD defects can be initiated from railhead surface or inside railhead from subsurface area, and for existing NDE methods including MFL method, the detection capability for surface defects and subsurface defects is different. Thus, a surface hemisphere-type defect and subsurface hole-type defect are both considered here. The simulated three-axis MFL signals are extracted with a spatial resolution of 0.2 mm, and the characteristics of three-axis MFL signals, including peak-to-peak values and spatial distribution, are analyzed.

The rest of this article is organized as follows. Section II presents the mechanism of MIEC effect on MFL method during high-speed rail inspection. Section III presents the 3-D FEM simulation models, results, and discussions, followed by conclusions and future work summarized in Section IV.

II. MECHANISM OF THE EFFECT OF MIEC

Generally, the rail track is made of carbon steel, which is a ferromagnetic material with high conductivity, and the permeability is determined by the nonlinear B – H curve. First, considering a static inspection, i.e., inspection speed is 0 mi/h, the rail is subjected to the applied dc magnetic field \vec{B}_A and is magnetized to its saturation state. The relationship between \vec{B}_A and applied magnetic field strength \vec{H}_A inside the rail is given by

$$\vec{B}_A = \mu \vec{H}_A = \mu_0 \mu_r \vec{H}_A = \mu_0 (\vec{H}_A + \vec{M}_A) \quad (1)$$

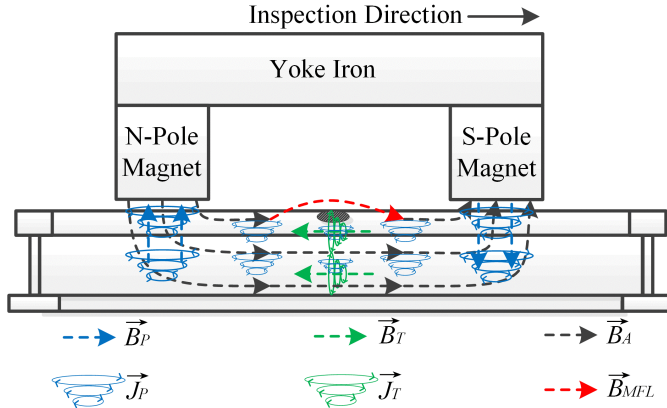


Fig. 1. Schematic of the effect of MIEC on the MFL method during high-speed rail inspection, J_P is MIEC generated near the two magnets and J_T is MIEC generated in the middle of the two magnets, \vec{B}_P and \vec{B}_T are secondary magnetic fields generated by J_P and J_T , respectively, \vec{B}_A is applied dc magnetic field, and \vec{B}_{MFL} is MFL field.

where \vec{M}_A is the magnetization of rail track, μ_0 is the permeability of vacuum, and μ_r is the relative permeability of rail track. The MFL field measured at point $r(x, y, z)$ in the 3-D Cartesian coordinate system using the magnetic dipole model for a defect can be expressed as [28]

$$\begin{aligned} \vec{B}_{MFL}(r) &= mfl(\vec{M}_A, r, s) = \frac{\mu_0}{4\pi} \left(\int_V \frac{-\nabla \cdot \vec{M}_A(s)}{|r-s|^3} (r-s) dV(s) \right. \\ &\quad \left. + \int_S \frac{n(s) \cdot \vec{M}_A(s)}{|r-s|^3} (r-s) dS(s) \right) \end{aligned} \quad (2)$$

where s is the point in the volume and on the surface of the rail defect and V and S denote the volume and surface of 3-D defect, respectively. Equation (2) indicates that the measured MFL signals are determined by three factors: magnetization of rail, sensor's measuring point, and defect profile.

Fig. 1 shows the schematic of the high-speed MFL inspection of the rail track. When performing high-speed rail inspection, according to Maxwell's equations, due to the relative motion between the two magnets and the rail, a time-varying magnetic field will induce an MIEC \vec{J}_T in the middle of the two magnets, which can be expressed as

$$\vec{J}_T = -\sigma \frac{\partial \vec{A}}{\partial t} \quad (3)$$

where σ is the electrical conductivity of the rail and \vec{A} is the magnetic vector potential. Meanwhile, when the two magnets move at a certain velocity \vec{V} relative to the rail, according to Faraday's law, another MIEC \vec{J}_P will be generated in the rail near the two magnet poles, which can be written as

$$\vec{J}_P = \sigma \vec{V} \times \vec{B}_A = \sigma \vec{V} \times \nabla \times \vec{A}. \quad (4)$$

Thus, the governing equation for MIEC in high-speed MFL inspection can be expressed as

$$\nabla \times \left(\frac{1}{\mu} \nabla \times \vec{A} \right) = \vec{J}_S - \sigma \frac{\partial \vec{A}}{\partial t} + \sigma \vec{V} \times \nabla \times \vec{A} \quad (5)$$

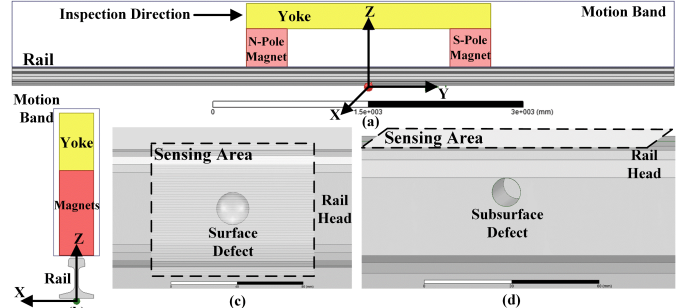


Fig. 2. 3-D simulation models for high-speed rail MFL inspection. (a) Front view, (b) right side view, (c) top view of surface hemisphere-type defect, and (d) front view of subsurface hole-type defect.

where \vec{J}_S is the source current density generated by the two magnets. As shown in Fig. 1, \vec{J}_T will generate the secondary magnetic field \vec{B}_T that is opposite to the applied dc magnetic field \vec{B}_A , which in turn decreases the magnetization of rail. Meanwhile, \vec{J}_P will generate the secondary magnetic field \vec{B}_P that is near the two magnets and affects the spatial distribution of the MFL field. The magnetization considering the effect of \vec{J}_T on high-speed MFL inspection is defined as follows:

$$\hat{\vec{M}}_A = \frac{\vec{B}_A + \vec{B}_T}{\mu_0} \left(1 - \frac{1}{\mu_r} \right). \quad (6)$$

Then, $\hat{\vec{B}}_{MFL}$ can be determined by $\hat{\vec{M}}_A$ by (2), and the distorted MFL field is the superimposed magnetic field of $\hat{\vec{B}}_{MFL}$ and \vec{B}_P as follows:

$$\vec{B}_{DMFL} = \hat{\vec{B}}_{MFL} + \vec{B}_P = mfl(\hat{\vec{M}}_A, r, s) + \vec{B}_P. \quad (7)$$

Based on the equations, for the high-speed rail MFL inspection, the motion between the two magnets and the rail will induce two types of MIEC, which will generate two corresponding secondary magnetic fields that decrease the magnetization of rail and affect the MFL field spatially. Thus, the above derivations explained qualitatively how the measured three-axis MFL signals are distorted by the MIEC, and the higher the speed, the more severe the degree of distortion is. The characteristics of these physical parameters, the distributions of MIEC, and the MFL field will be further studied quantitatively through 3-D FEM simulations.

III. 3-D FEM SIMULATION MODELING

A. Simulation Setup

The 3-D FEM simulations are conducted by Ansys Maxwell software. The simulation models are shown in Fig. 2. The main simulation parameters and model structure parameters are listed in Tables II and III, respectively. Here, the combination of permanent magnets and yoke is selected to generate a dc magnetic circuit to magnetize the rail track. In addition, the alternative solution using an electromagnet, including excitation coils and yokes, can also be used to magnetize the rail track, as reported in [13] and [14]. The magnetizer, including N-pole and S-pole magnets and yoke, is located above the railhead with a liftoff value of 5 mm. The magnetizer is inside the motion band to generate a relative motion between

TABLE II
MAIN SIMULATION PARAMETERS SETTING

Conductivity of Rail	Magnetic Coercivity of Magnets	Relative Permeability of Yoke
5×10^6 S/m	7.2×10^5 A/m	1000

TABLE III
MODEL STRUCTURE PARAMETERS SETTING

Parameters	Values
Length of rail	7 m
Height of rail	175 mm
Width of rail foot	150 mm
Width of rail head	72 mm
Length of magnet	400 mm
Height of magnet	370 mm
Length of yoke	2.4 m
Height of yoke	250 mm
Width of magnet and yoke	150 mm
Distance between two poles	2 m
Length of sensing area along y-axis	100 mm
Width of sensing area along x-axis	50 mm
Radius of hemisphere-type defect	10 mm
Depth of hemisphere-type defect	6 mm
Radius of hole-type defect	5 mm
Height of hole-type defect	36 mm
Depth of hole-type defect	10 mm
Inspection speed	0, 12.5, 25, 37.5, 50, 62.5 mph

the magnetizer and the rail. The inspection direction of the magnetizer is along the positive Y -axis horizontal direction. The three-axis magnetic sensors are located at the sensing area with a liftoff value of 1 mm, which is at the center of the two magnetic poles and above the railhead to measure the simulated three-axis MFL signals. The three-axis MFL signals include transverse component \vec{B}_X , horizontal component \vec{B}_Y , and vertical component \vec{B}_Z , which are usually used as data inputs of inversion techniques to quantify defect size and profile. As shown in Fig. 2(c) and (d), a case of hemisphere-type defect is introduced to represent surface-initiated RCD defects, whereas a case of hole-type defect is introduced to represent subsurface-initiated RCD defects. It has been considered as high-speed rail inspection when the inspection speed exceeds 50 mi/h [13], [14]. Thus, the inspection speed adopted in the simulations ranges from 0 mi/h (static inspection) to 62.5 mi/h (high speed) with an interval of 12.5 mi/h. Fig. 3 shows the nonlinear B - H curve as well as relative permeability curve of the rail set in the simulations.

B. MIEC and Magnetic Fields in Rail Track

Fig. 4 shows the distribution of MIEC on the rail surface along the rail horizontal direction when the inspection speed is from 0 to 62.5 mi/h, whereas Fig. 5 shows the distribution of magnetic fields in the rail track. When performing static inspection at speed of 0 mi/h, the magnitude of MIEC is equal to zero in the rail so that MIEC has no effect on the magnetization of rail, making the magnetic field distribution almost symmetrical with respect to the two magnets, and the

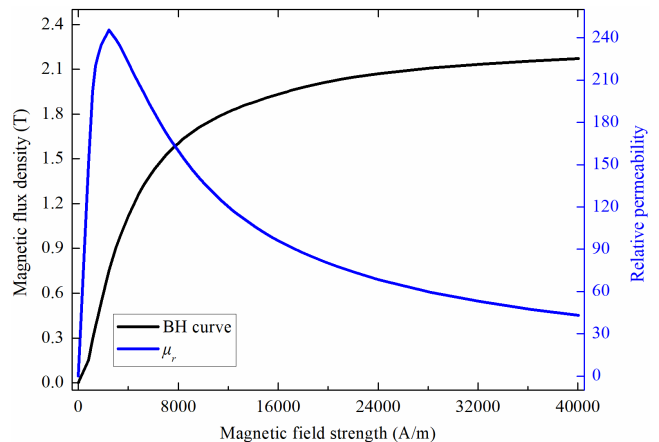


Fig. 3. Nonlinear B - H curve of the rail.

rail is magnetized to its saturation state with magnetic flux density exceeding 1.8 T, which can be seen in Fig. 5(a). With the increase of speed, the distribution area and magnitude of MIEC increase, especially there is more MIEC distributed on both sides of the two magnets as well as near the defect area marked by the dotted circle shown in Fig. 4. For the cases from Fig. 5(b)–(f), due to the existence of MIEC including \vec{J}_T and \vec{J}_P , the magnetic field in the rail is the superposition of \vec{B}_A , \vec{B}_T , and \vec{B}_P . For high-speed rail inspection with the speeds of 50–62.5 mi/h, the magnetization of the rail near the defect area decreases significantly, causing the weakly magnetized regions inside the railhead and the rail foot, shown as dotted circles in Fig. 5(e) and (f).

Fig. 6 shows the distribution of magnetic fields in the transverse section of the rail when the inspection speed is from 0 to 62.5 mi/h. As the speed increases, the magnetization inside the railhead and rail foot gradually decreases, forming two elliptical weakly magnetized regions inside the rail (marked as dotted area). The reason is that more MIEC will be induced in the middle of the two magnets near the defect area with the increase of speed, thereby generating secondary magnetic fields that reduce the magnetization of the rail. In high-speed rail MFL inspection, since the subsurface defect and the weakly magnetized regions inside the railhead are partially overlapped, the MFL signals from the subsurface defect will be more affected by the weakly magnetized regions comparing to the surface defect.

Figs. 7–9 show the 3-D distribution of MIEC along the rail transverse section (right side view) when the inspection speed is 62.5 mi/h to illustrate the main cause of the inner weakly magnetized regions as well as the effect of MIEC on the MFL measurement. Fig. 7 shows the vector components of MIEC for the surface and subsurface defects. The distribution of MIEC has two main directions: one is \vec{J}_T distributed in the rail transverse section along the clockwise direction marked as dashed circle, and the other is \vec{J}_P flowing in on the left side and flowing out on the right side marked as circle dot and circle cross. Figs. 8 and 9 show the distribution of \vec{J}_T and \vec{J}_P , respectively. \vec{J}_T is mainly concentrated in the two regions inside railhead and rail foot. According to the right-hand rule, \vec{J}_T will generate the secondary magnetic field \vec{B}_T that is along

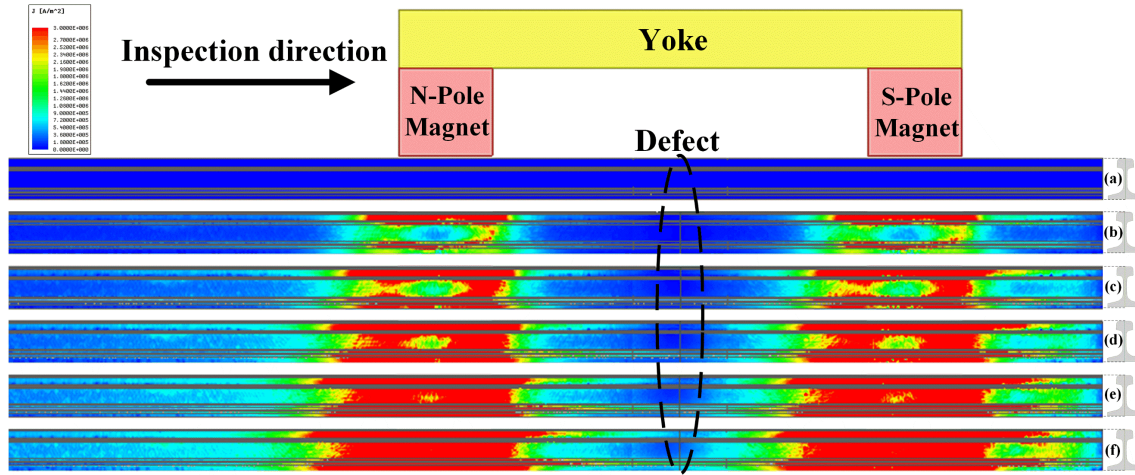


Fig. 4. Distribution of MIEC on the rail surface along the rail horizontal direction at different inspection speeds: (a) 0, (b) 12.5, (c) 25, (d) 37.5, (e) 50, and (f) 62.5 mi/h.

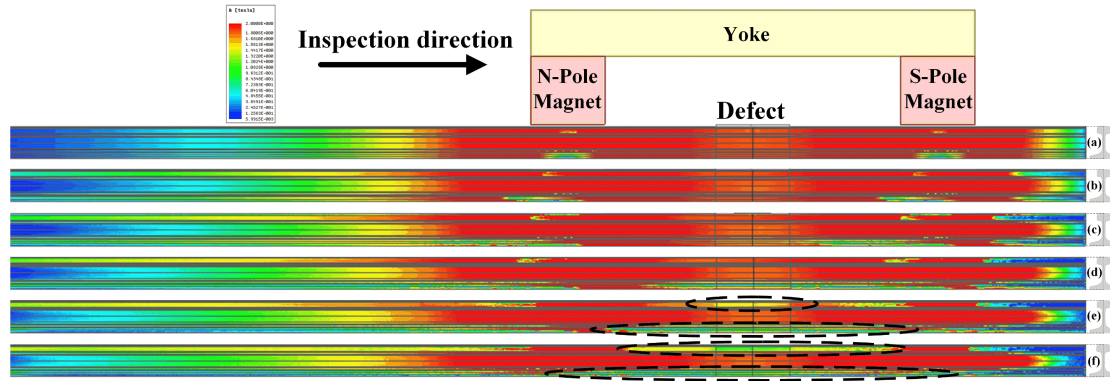


Fig. 5. Distribution of magnetic flux density in the longitudinal central section of the rail at different inspection speeds: (a) 0, (b) 12.5, (c) 25, (d) 37.5, (e) 50, and (f) 62.5 mi/h.

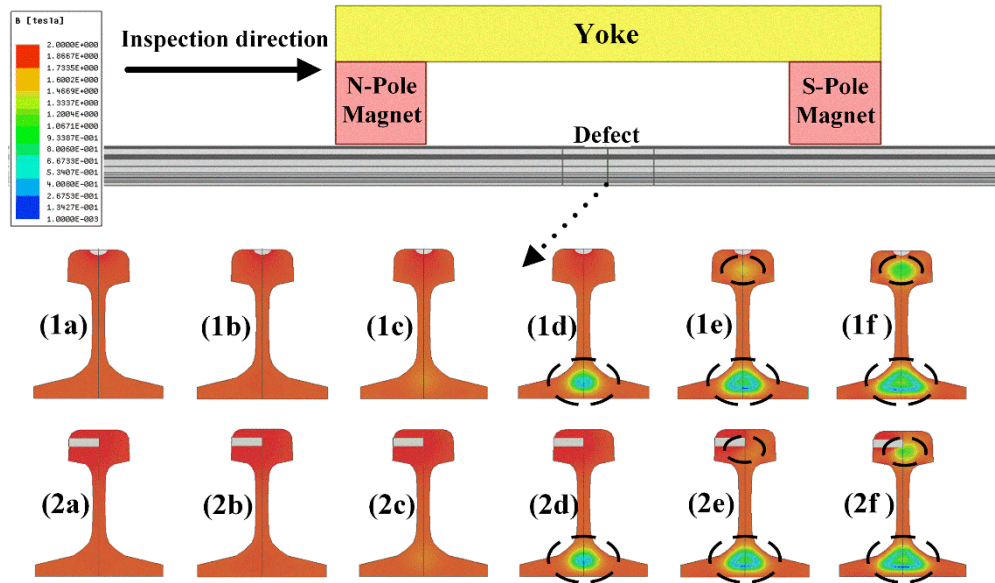


Fig. 6. Distribution of magnetic fields in the transverse section of the rail at the center of the defect during different inspection speeds: (1a)–(1f) surface defect cases when the speed is from 0 to 62.5 mi/h, respectively and (2a)–(2f) subsurface defect cases when the speed is from 0 to 62.5 mi/h, respectively.

the negative Y -axis (horizontal) direction, which is opposite to the dc applied magnetic field \vec{B}_A , so that the distribution of \vec{J}_T is the main cause of forming the two weakly magnetized

regions shown in Fig. 6. It is worth noting that, compared with the surface defect, the MFL signals from the subsurface defect will be more affected by the weakly magnetized region inside

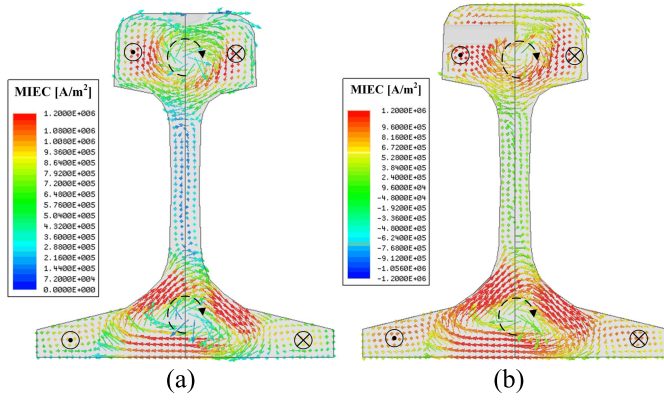


Fig. 7. Vector component of MIEC in the rail transverse section (right side view) at the center of defect. (a) Surface defect. (b) Subsurface defect.

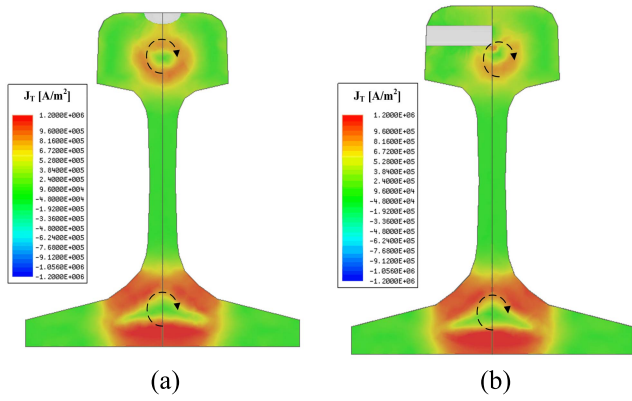


Fig. 8. Distribution of \vec{J}_T in the rail transverse section at the center of defect. (a) Surface defect. (b) Subsurface defect.

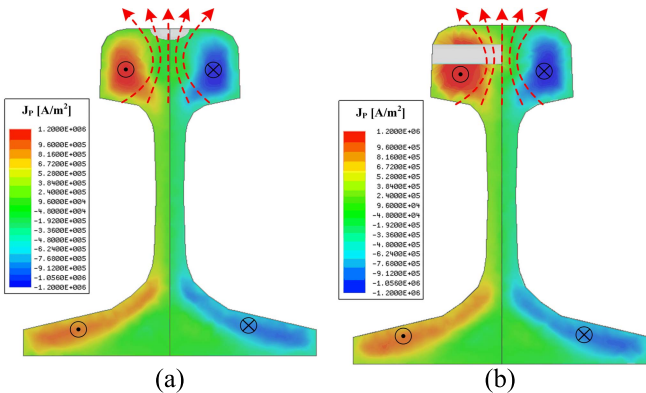
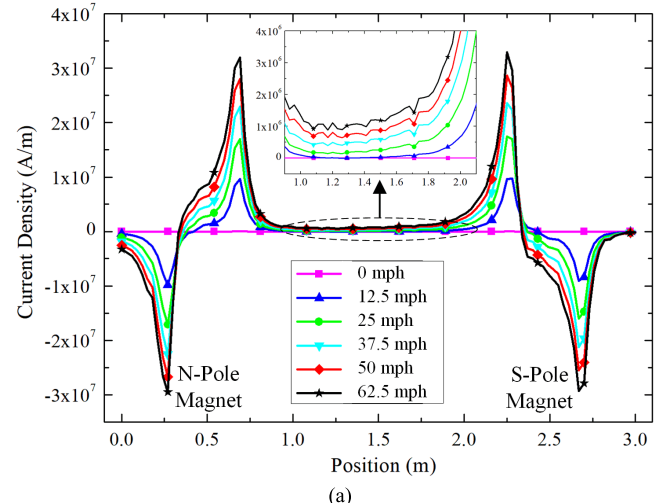


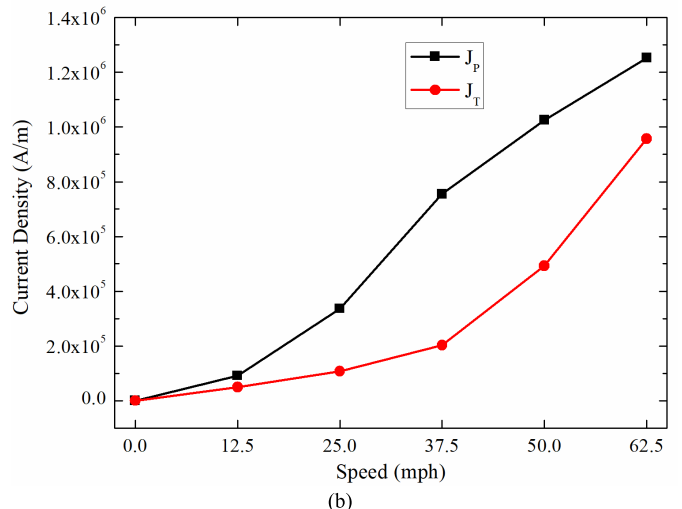
Fig. 9. Distribution of \vec{J}_P in the rail transverse section at the center of defect. (a) Surface defect. (b) Subsurface defect.

railhead caused by \vec{J}_T . As shown in Fig. 9, the distribution of \vec{J}_P will generate the secondary magnetic field \vec{B}_P (marked as red dashed arrows) distributed from the inside of railhead to space above the railhead along the X-axis (transverse) and Z-axis (vertical) directions, which has little impact on the magnetization of rail; however, it will affect the spatial distribution of MFL field along the X- and Z-axes.

Fig. 10 shows the magnitudes of \vec{J}_T and \vec{J}_P changing with different rail positions and inspection speeds. According to the previous mechanism analysis, \vec{J}_P is generated near



(a)



(b)

Fig. 10. Magnitudes of \vec{J}_T and \vec{J}_P change with different positions and speeds. (a) \vec{J}_P changes with rail positions along the Y-axis horizontal direction. (b) \vec{J}_T and \vec{J}_P change with inspection speeds at the center of the two magnets (at rail position of 1.5 m).

the two magnets. Fig. 10(a) shows that \vec{J}_P is concentrated near the two magnets and has the four opposite peak values at both sides of the two magnets. Here, the positive value indicates that the direction of \vec{J}_P is flowing in on the left side and flowing out on the right side as shown in Fig. 9, whereas the negative value indicates the opposite direction. It is worth noting that the opposite peak values of \vec{J}_P near the two magnet poles also indicate that the MIEC directions near the N-pole and the S-pole are opposite. Meanwhile, with the increase of speed, the magnitude of \vec{J}_P increases at different rail positions. It is noted that \vec{J}_P will be induced and decay over time, rather than disappear immediately, which means that as the magnetizer moves forward along the Y-axis horizontal direction, the position of previous induced \vec{J}_P will be changed from the S-pole magnet to the center of the two magnetics. In Fig. 10(a), the enlarged subfigure shows that the magnitude of \vec{J}_P at the position of 1.5 m (defect area) is not equal to zero; however, the order of magnitude is reduced from 10⁷ to 10⁶ A/m, and the higher the speed, the higher the magnitude. This simulation result indicates that the distributed \vec{J}_P shown

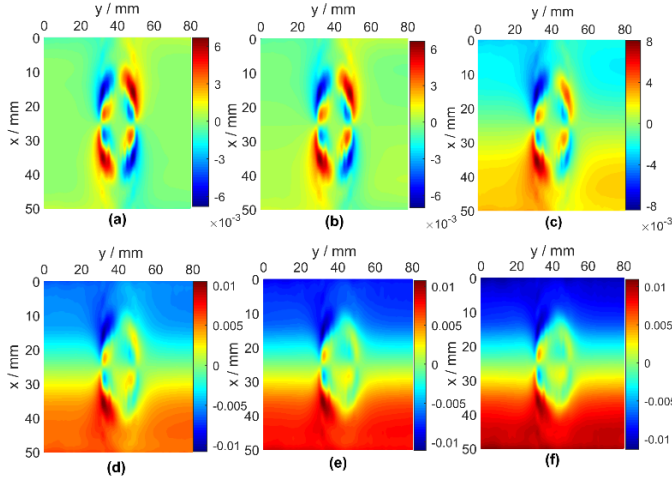


Fig. 11. 2-D \vec{B}_X from the surface defect at different speeds: (a) 0, (b) 12.5, (c) 25, (d) 37.5, (e) 50, and (f) 62.5 mi/h.

in Fig. 9 is a result of the strong induced \vec{J}_P near the S-pole magnet gradually decreasing as the magnetizer moves forward. This phenomenon is also shown in Fig. 1 by the several blue circles in the rail track along the horizontal direction. \vec{B}_P , which can affect that the spatial distribution of MFL fields is generated by \vec{J}_P located at the center of the two magnets rather than that near the two magnet poles. Fig. 10(b) shows \vec{J}_T and \vec{J}_P changes with inspection speeds at the center of the two magnets with a position of 1.5 m. The relationships between \vec{J}_P and \vec{J}_T versus inspection speeds can be described as linearly and exponentially correlated, respectively.

C. Three-Axis MFL Signals

As discussed above, \vec{J}_T and \vec{J}_P near the defect area generate secondary magnetic fields \vec{B}_T and \vec{B}_P , respectively, where \vec{B}_T decreases the magnetization in railhead that affects MFL signals from the subsurface defect, whereas \vec{B}_P affects the spatial distribution of MFL field, especially along the X - and Z -axes. Fig. 11 shows the transverse X -axis component of three-axis MFL signals \vec{B}_X collected from the sensing area from the surface hemisphere-type defect shown in Fig. 2, while 1-D \vec{B}_X is extracted from Fig. 11 at $x = 35$ mm (where peak values exist) along the Y -axis horizontal direction to draw Fig. 12. Then, Fig. 13 shows \vec{B}_X from the subsurface hole-type defect, while 1-D \vec{B}_X is extracted from Fig. 13 at $x = 45$ mm to draw Fig. 14. As shown in Figs. 11 and 13, with the increase of speed, \vec{B}_X are interfered by strong background signals on both sides $[(x < 20 \text{ mm}) \cup (x > 30 \text{ mm})]$, which can also be reflected by the increase of the base values in Figs. 12 and 14. The reason is that the secondary magnetic field \vec{B}_P generated by \vec{J}_P can affect the spatial distribution of MFL field along the X -axis direction, and the higher the speed, the greater the magnitudes of \vec{J}_P and \vec{B}_P , so the higher the base values of \vec{B}_X . Meanwhile, Fig. 14 shows that the peak-to-peak values of \vec{B}_X from the subsurface defect decrease significantly with the increase of speed; however, the peak-to-peak values of \vec{B}_X from the surface defect change little with the increase of speed. Because only the subsurface defect is partially overlapped with the weakly magnetized regions

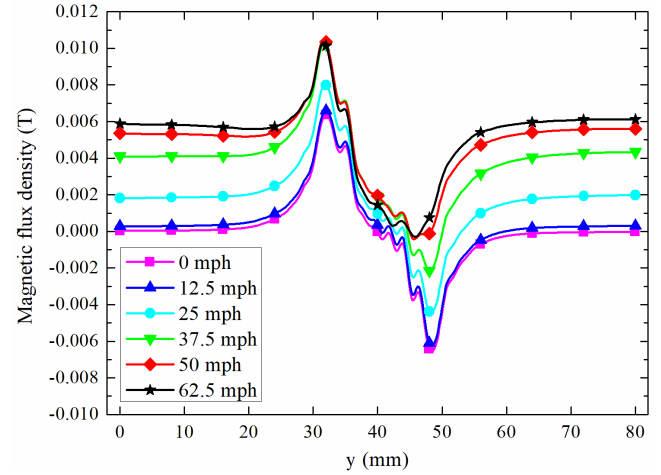


Fig. 12. 1-D \vec{B}_X extracted from Fig. 11 from the surface defect at $x = 35$ mm at different speeds.

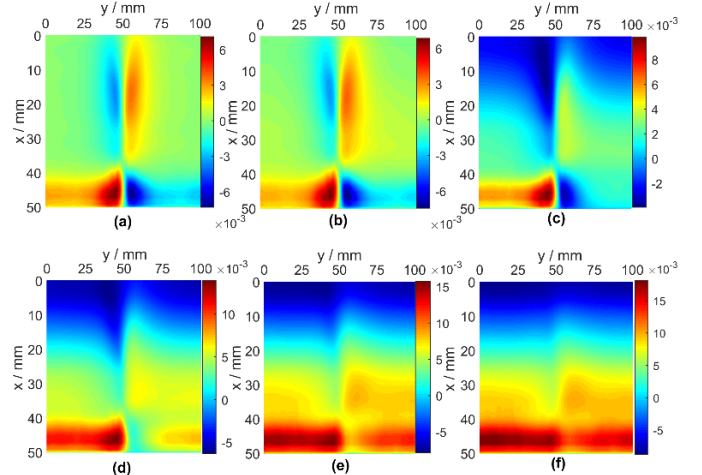


Fig. 13. 2-D \vec{B}_X from the subsurface defect at different speeds: (a) 0, (b) 12.5, (c) 25, (d) 37.5, (e) 50, and (f) 62.5 mi/h.

caused by \vec{J}_T and \vec{B}_T inside railhead so that the higher the speed, the greater the magnitudes of \vec{J}_T and \vec{B}_T , and the lower the magnetization inside railhead, so the lower the peak-to-peak values from the subsurface defect. The surface defect is less affected by the weakly magnetized regions so that \vec{J}_T has little effect on the peak-to-peak values from the surface defect.

Next, \vec{B}_Y and \vec{B}_Z from the surface and subsurface defects, including 2-D images and 1-D curves, are shown from Figs. 15–22. These results show that the peak-to-peak values of \vec{B}_Y and \vec{B}_Z from the subsurface defect decrease significantly with the increase of speed, while those from the surface defect change little with the increase of speed, which has the same trend as \vec{B}_X . Then, since the secondary magnetic field \vec{B}_P generated by \vec{J}_P affects the spatial distribution of MFL field along the X - and Z -axes except for the Y -axis, the base values of \vec{B}_X and \vec{B}_Z increase with the increase of speeds, but those of \vec{B}_Y change little with the increase of speed.

D. Discussion

According to the simulation results, the effect of MIEC on the three-axis MFL signals for high-speed rail inspection has

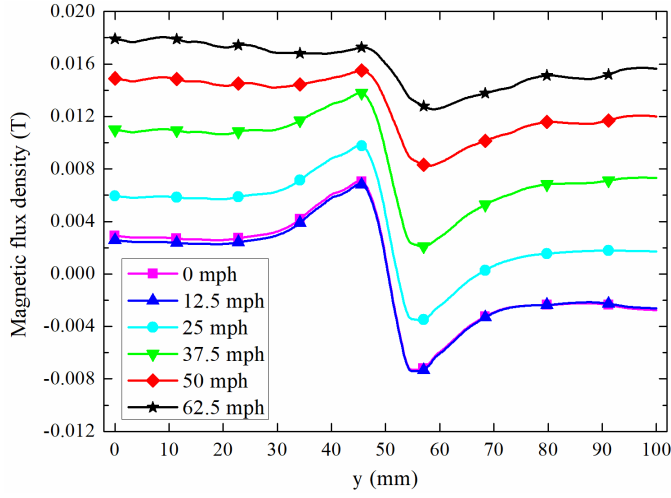


Fig. 14. 1-D \vec{B}_X extracted from Fig. 13 from the subsurface defect at $x = 45$ mm at different speeds.

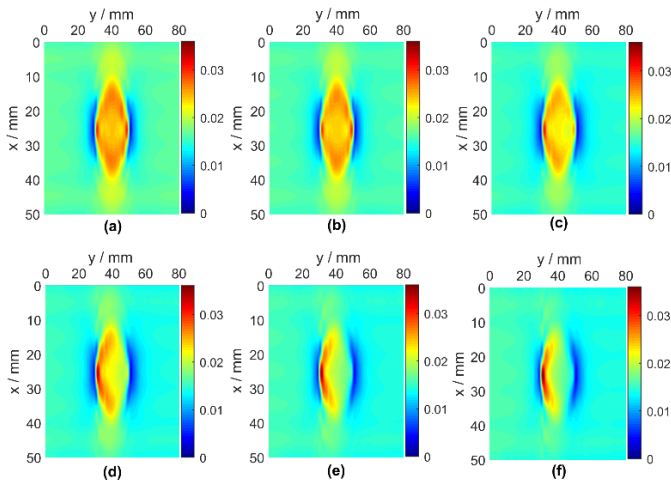


Fig. 15. 2-D \vec{B}_Y from the surface defect at different speeds: (a) 0, (b) 12.5, (c) 25, (d) 37.5, (e) 50, and (f) 62.5 mi/h.

two main aspects: one is increasing the base values of \vec{B}_X and \vec{B}_Z from the surface and subsurface defects, and the other is decreasing the peak-to-peak values of three-axis MFL signals from the subsurface defect. From the perspective of signal processing, the impact of base values can be mitigated directly through subtracting base values from MFL measurements to obtain high SNR MFL defect signals. Take \vec{B}_X from the surface defect as an example, and Fig. 23 shows the MFL defect signals obtained by subtracting the base values [$y = 0$ and $x \in (0, 50)$] from B_X in Fig. 11 for each speed. The background signals on both sides disappear, and the sphere-type defect profile is clearly displayed.

Fig. 24 shows the peak-to-peak values of three-axis MFL signals from the surface and subsurface defects changing with inspection speed. The peak-to-peak value of \vec{B}_Y from the subsurface defect reduces from 0.044 T at 0 mi/h to 0.011 T at 62.5 mi/h, while that of \vec{B}_Z reduces from 0.05 to 0.016 T, resulting a decrease of more than 70%. The downward trend in this article is similar to the result in [14] that the magnitude of MFL signals reduces about 64% when the inspection speed

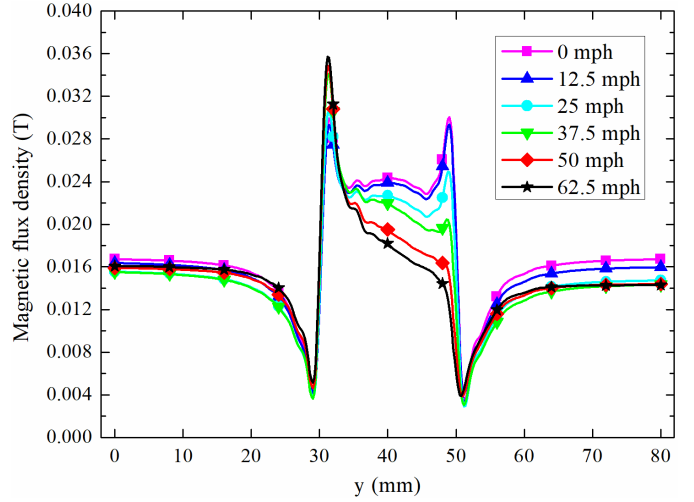


Fig. 16. 1-D \vec{B}_Y extracted from Fig. 15 from the surface defect at $x = 25$ mm at different speeds.

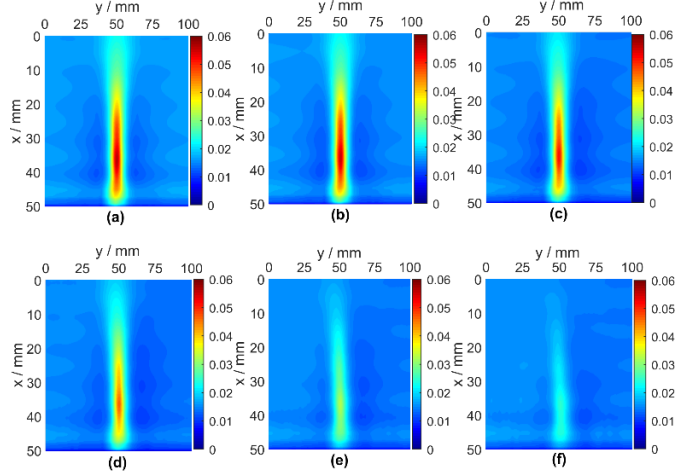


Fig. 17. 2-D \vec{B}_Y from the subsurface defect at different speeds: (a) 0, (b) 12.5, (c) 25, (d) 37.5, (e) 50, and (f) 62.5 mi/h.

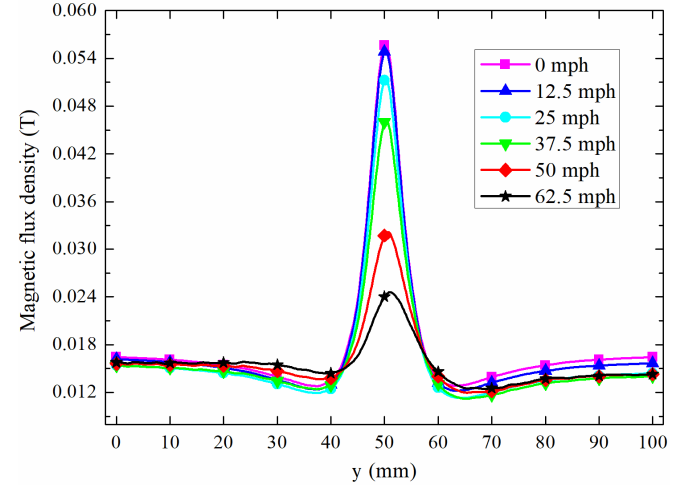


Fig. 18. 1-D \vec{B}_Y extracted from Fig. 17 from the subsurface defect at $x = 35$ mm at different speeds.

is from 20 to 50 mi/h for the subsurface hole-type defects through the on-site high-speed rail MFL experiments. Then, a 70% decrease in magnitude will cause about 10-dB decrease

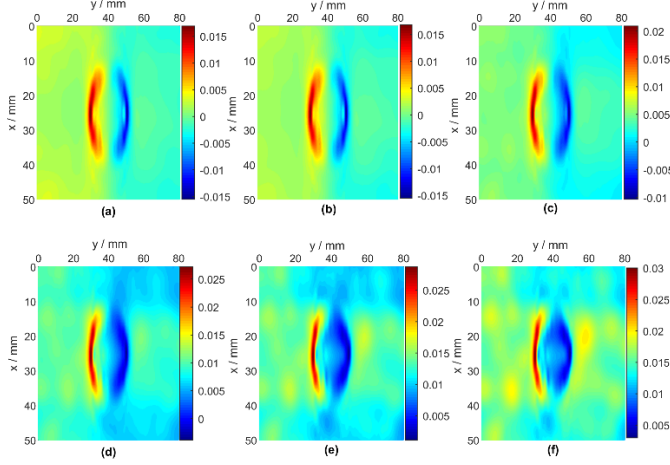


Fig. 19. 2-D \vec{B}_Z from the surface defect at different speeds: (a) 0, (b) 12.5, (c) 25, (d) 37.5, (e) 50, and (f) 62.5 mi/h.

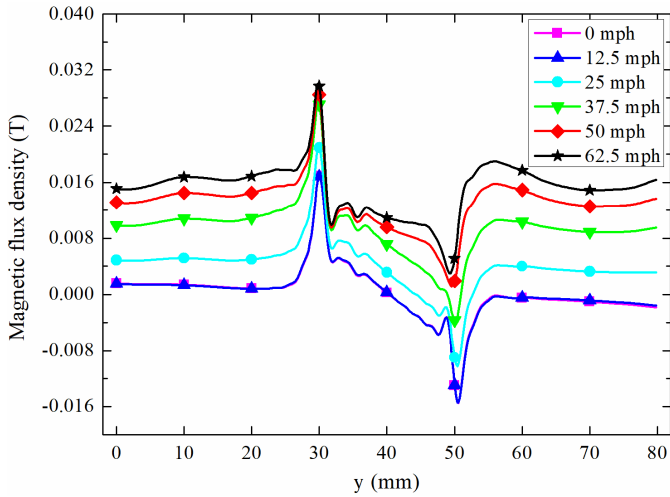


Fig. 20. 1-D \vec{B}_Z extracted from Fig. 19 from the surface defect at $x = 25$ mm at different speeds.

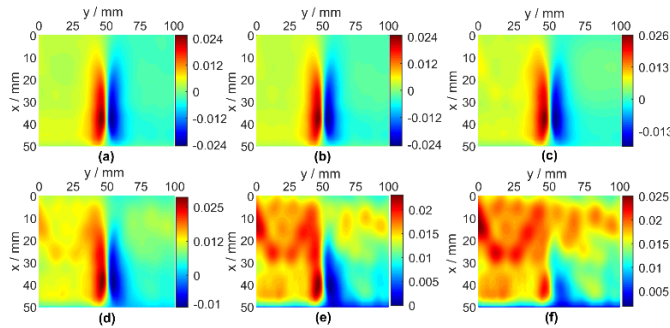


Fig. 21. 2-D \vec{B}_Z from the subsurface defect at different speeds: (a) 0, (b) 12.5, (c) 25, (d) 37.5, (e) 50, and (f) 62.5 mi/h.

in SNR. The decrease in SNR is caused by the loss of useful information, rather than interference with background noises so that it is difficult to mitigate and recover through filtering, resulting in a significant decrease in the sensitivity and specificity of MFL measurements.

In addition, \vec{B}_X in Fig. 23, \vec{B}_Y in Fig. 16, and \vec{B}_Z in Fig. 19 from the surface defect show that MFL signals are

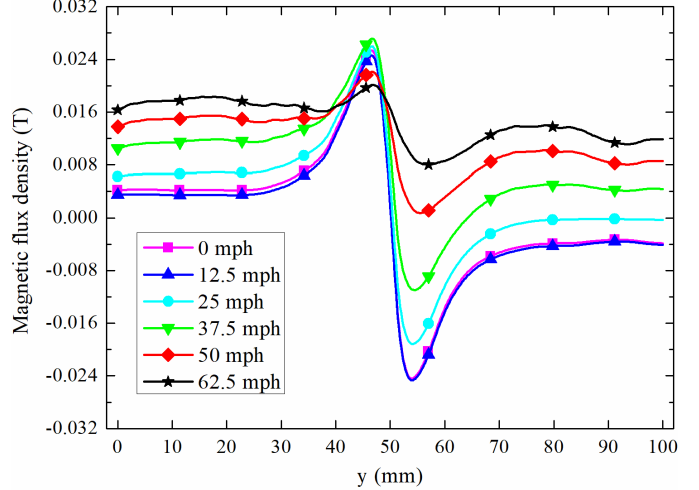


Fig. 22. 1-D \vec{B}_Z extracted from Fig. 21 from the subsurface defect at $x = 40$ mm at different speeds.

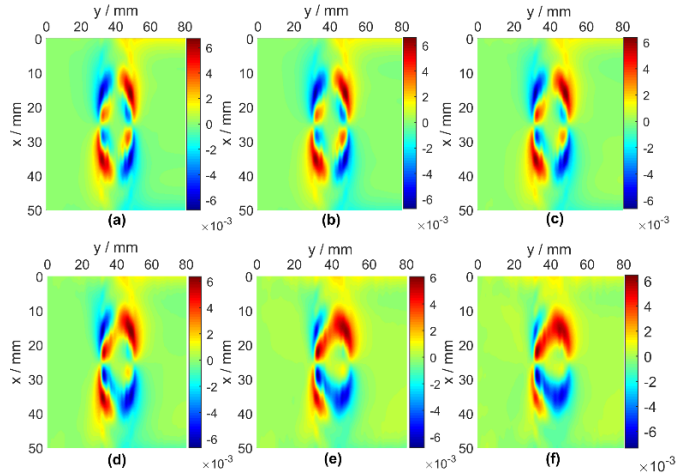


Fig. 23. 2-D MFL defect signals of \vec{B}_X obtained from Fig. 11 by subtracting base values at different speeds: (a) 0, (b) 12.5, (c) 25, (d) 37.5, (e) 50, and (f) 62.5 mi/h.

asymmetric along the horizontal Y -axis direction, especially near the peaks on both sides of defect profile. The higher the speed, the stronger the degree of asymmetry. This asymmetric phenomenon from the surface defects on railhead is also reported in [13] and [21] but lack of cause analysis. Fig. 25 shows the vector component of MIEC on the surface defect profile (top view) when the speed is 62.5 mi/h. The reason is that high-speed motion will cause the asymmetric distribution of MIEC around the defect area, especially on the defect profile along the horizontal Y -axis direction. The magnitude of MIEC on the left side is greater than that on the right side, so the asymmetric secondary magnetic fields will be generated in the space above railhead and superimposed on the MFL field, resulting in the asymmetry in MFL measurements. The signal distortion caused by the asymmetry will also have a certain degree of impact on the defect characterization, especially in reconstructing the defect profile during the high-speed rail MFL inspection.

The simulation results indicate that MFL measurements will have high SNR and sensitivity from surface and subsurface

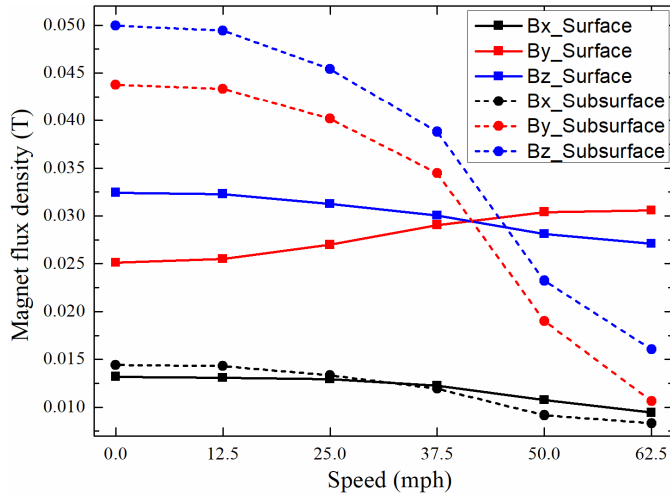


Fig. 24. Peak-to-peak values of three-axis MFL signals from surface and subsurface defects at different speeds.

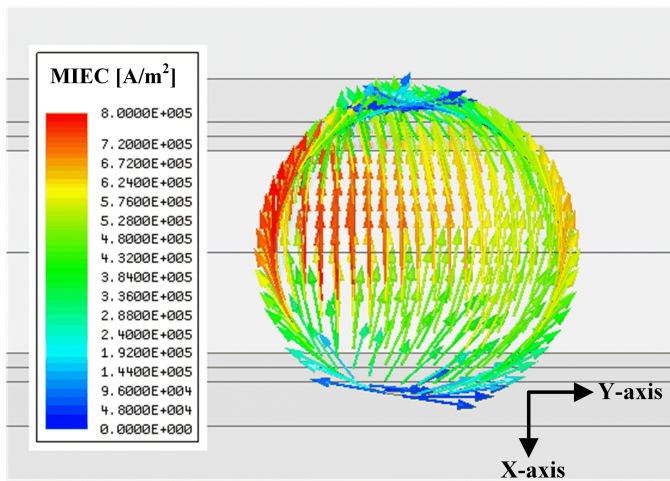


Fig. 25. Vector component of MIEC on the surface defect profile when the speed is 62.5 mi/h.

defects on railhead when inspection speed is lower than 25 mi/h. Thus, in practice, MFL is one of the optimal methods to detect surface and subsurface RCD defects for the low-speed inspection systems, including portable devices or hi-rail vehicles. However, for high-speed inspection using inspection trains with speeds exceeding 50 mi/h, the effect of MIEC on MFL measurements is nonnegligible. For the distortions of MFL measurements, the shift of base values is relatively easy to eliminate. In contrast, it is required to utilize high-sensitivity magnetic sensors and data compensation technologies to mitigate the negative effect on defect characterization and assessment caused by the asymmetry from surface RCD defects and the reduction in magnitude from subsurface RCD defects.

IV. CONCLUSION

High-speed and high-accuracy inspection of rail defects using NDT methods is essential to the efficiency and safety of railway transportation. The existing MFL method suffers from the effect of MIEC that the measured three-axis MFL signals are severely distorted. There is a lack of mechanical analyses

on the effect of MIEC, and the underlying causes of distortion are not well understood. This article thoroughly investigates the effect of MIEC on three-axis MFL signals for high-speed rail inspection through 3-D FEM simulations, and the relationships between MIEC distributions and MFL measurements are presented and analyzed. The motion between the magnetizer and the rail will generate two types of MIEC, including \vec{J}_T and \vec{J}_P . \vec{J}_T will generate the secondary magnetic field \vec{B}_T that is opposite to the dc applied magnetic field \vec{B}_A , forming the weakly magnetized region inside the railhead, which in turn decreases the peak values of three-axis MFL signals from the subsurface defect. \vec{J}_P will generate \vec{B}_P that affects the spatial MFL signals, especially the base values along rail transverse and vertical directions. The effect of MIEC on the three-axis MFL signals in terms of SNR, sensitivity, and asymmetry is also analyzed. The future work will focus on the high-speed rail MFL simulations and experimental validations, especially for different RCD defect sizes, orientations, and small cracks, as well as data inversion algorithms based on the measured three-axis MFL signals to quantify defect sizes and reconstruct defect profiles.

ACKNOWLEDGMENT

This work was supported in part by the AAR Strategic Research Initiative (SRI) University Program. The authors would like to thank the support of the Association of American Railroads/Transportation Technology Center, Inc. (AAR/TTCI) and Dr. Gary Fry who oversees the research program. They would also like to thank Dr. Anish Poudel for his valuable comments.

REFERENCES

- [1] Central Intelligence Agency. *The World Factbook*. Accessed: 2019. [Online]. Available: <https://www.cia.gov/the-world-factbook/field/railways/country-comparison>
- [2] *Railway safety statistics in the EU*. Accessed: Dec. 1, 2020. [Online]. Available: https://ec.europa.eu/eurostat/statistics-explained/index.php?title=Railway_safety_statistics_in_the_EU
- [3] *Chinese Railway Safety Assessment Annual Report*. Accessed: 2019. [Online]. Available: <http://www.nra.gov.cn/jgzf/zfjg/zfdt>
- [4] *United States Federal Railroad Administration Office of Safety Analysis*. Accessed: Nov. 30, 2020. [Online]. Available: <https://safetydata.fra.dot.gov/officeofsafety/publicsites/Query/TrainAccidentDamage.aspx>
- [5] M. Steenbergen, "Rolling contact fatigue: Spalling versus transverse fracture of rails," *Wear*, vols. 380–381, pp. 96–105, Jun. 2017.
- [6] D. F. Cannon, K. O. Edel, S. L. Grassie, and K. Sawley, "Rail defects: An overview," *Fatigue Fract. Eng. Mater. Struct.*, vol. 26, no. 10, pp. 865–886, Oct. 2003.
- [7] M. Ph Papaefthimiou, C. Roberts, and C. L. Davis, "A review on non-destructive evaluation of rails: State-of-the-art and future development," *Proc. Inst. Mech. Eng. F. J. Rail Rapid Transit*, vol. 222, no. 4, pp. 367–384, Jul. 2008.
- [8] Z. Osama, S. Shihab, and W. Al-Nuaimy, "Recent developments in ultrasonic techniques for rail-track inspection," in *Proc. Annu. Conf. Brit. Inst. Non-Destructive Test.*, 2002, pp. 55–60.
- [9] H.-M. Thomas, T. Heckel, and G. Hanspach, "Advantage of a combined ultrasonic and eddy current examination for railway inspection trains," *Insight Non-Destructive Test. Condition Monitor*, vol. 49, no. 6, pp. 341–344, Jun. 2007.
- [10] A. Poudel, B. Lindeman, and R. Wilson, "Current practices of rail inspection using ultrasonic methods: A review," *Mater. Eval.*, vol. 77, no. 7, pp. 870–883, 2019.
- [11] S. Dixon, R. S. Edwards, and X. Jian, "Inspection of rail track head surfaces using electromagnetic acoustic transducers (EMATs)," *Insight Non-Destructive Test. Condition Monitor*, vol. 46, no. 6, pp. 326–330, Jun. 2004.

- [12] J. L. Rose, M. J. Avioli, P. Mudge, and R. Sanderson, "Guided wave inspection potential of defects in rail," *NDT E Int.*, vol. 37, no. 2, pp. 153–161, Mar. 2004.
- [13] Y. Li, G. Y. Tian, and S. Ward, "Numerical simulation on magnetic flux leakage evaluation at high speed," *NDT E Int.*, vol. 39, no. 5, pp. 367–373, Jul. 2006.
- [14] A. G. Antipov and A. A. Markov, "3D simulation and experiment on high speed rail MFL inspection," *NDT E Int.*, vol. 98, pp. 177–185, Sep. 2018.
- [15] J. Rajamäki, M. Vippola, A. Nurmi, and T. Viitala, "Limitations of eddy current inspection in railway rail evaluation," *Proc. Inst. Mech. Eng. F. J. Rail Rapid Transit*, vol. 232, no. 1, pp. 121–129, Jan. 2018.
- [16] G. Piao, J. Guo, T. Hu, Y. Deng, and H. Leung, "A novel pulsed eddy current method for high-speed pipeline inline inspection," *Sens. Actuators A, Phys.*, vol. 295, pp. 244–258, Aug. 2019.
- [17] Q. Li and S. Ren, "A real-time visual inspection system for discrete surface defects of rail heads," *IEEE Trans. Instrum. Meas.*, vol. 61, no. 8, pp. 2189–2199, Aug. 2012.
- [18] A. M. Poudel MWitte, P. Gies, and D. Skow, "Rolling contact damage characterization on railroad rails using electromagnetic field imaging," *Mater. Eval.*, vol. 77, no. 7, pp. 951–965, 2019.
- [19] G. Y. Tian, B. Gao, Y. L. Gao, P. Wang, H. T. Wang, and Y. S. Shi, "Review of railway rail defect non-destructive testing and monitoring," *Chin. J. Sci. Instrum.*, vol. 37, no. 8, pp. 1763–1780, 2016.
- [20] M. Witte, and A. Poudel, "Review of wayside detection and monitoring technologies and their future for North American railroad applications," *Mater. Eval.*, vol. 77, no. 7, pp. 885–896, 2019.
- [21] Z. Chen, J. Xuan, P. Wang, H. Wang, and G. Tian, "Simulation on high speed rail magnetic flux leakage inspection," in *Proc. IEEE Int. Instrum. Meas. Technol. Conf.*, May 2011, pp. 1–5.
- [22] G. S. Park and S. H. Park, "Analysis of the velocity-induced eddy current in MFL type NDT," *IEEE Trans. Magn.*, vol. 40, no. 2, pp. 663–666, Mar. 2004.
- [23] J. Wu, Y. Sun, B. Feng, and Y. Kang, "The effect of motion-induced eddy current on circumferential magnetization in MFL testing for a steel pipe," *IEEE Trans. Magn.*, vol. 53, no. 7, pp. 1–6, Jul. 2017.
- [24] G. Piao, J. Guo, T. Hu, and H. Leung, "The effect of motion-induced eddy current on high-speed magnetic flux leakage (MFL) inspection for thick-wall steel pipe," *Res. Nondestruct. Eval.*, vol. 31, no. 1, pp. 48–67, Jan. 2020.
- [25] T. J. Rocha, H. G. Ramos, A. L. Ribeiro, and D. J. Pasadas, "Evaluation of subsurface defects using diffusion of motion-induced eddy currents," *IEEE Trans. Instrum. Meas.*, vol. 65, no. 5, pp. 1182–1187, May 2016.
- [26] J. Wu, J. Zhu, G. Tian, H. Xia, X. Huang, and C. Tang, "Study of rotating magnet array-based motion-induced eddy current thermography," *IEEE Trans. Magn.*, vol. 54, no. 12, pp. 1–5, Dec. 2018.
- [27] P. Wang, Y. Gao, G. Tian, and H. Wang, "Velocity effect analysis of dynamic magnetization in high speed magnetic flux leakage inspection," *NDT E Int.*, vol. 64, pp. 7–12, Jun. 2014.
- [28] S. Hosseingholizadeh, T. Filletter, and A. N. Sinclair, "Evaluation of a magnetic dipole model in a DC magnetic flux leakage system," *IEEE Trans. Magn.*, vol. 55, no. 4, pp. 1–7, Apr. 2019.

Guanyu Piao received the B.S. degree in electrical engineering from Jilin University, Changchun, China, in 2014, and the Ph.D. degree in electrical engineering from Tsinghua University, Beijing, China, in 2019.

He is currently a Post-Doctoral Research Associate with the Nondestructive Evaluation Laboratory, Electrical and Computer Engineering Department, College of Engineering, Michigan State University, East Lansing, MI, USA. His current research interests include electromagnetic, ultrasonic, and optical nondestructive testing and evaluation (NDT&E), applied electromagnetics, machine learning algorithms, and computational modeling and development of various NDT systems.

Jiaoyang Li received the B.S. degree in instrument science and technology from Jilin University, Changchun, China, in 2014, and the Ph.D. degree in electromagnetic field and microwave technology from the University of Chinese Academy of Sciences, Beijing, China, in 2019.

She is currently a Post-Doctoral Research Associate with the Nondestructive Evaluation Laboratory, Electrical and Computer Engineering Department, College of Engineering, Michigan State University, East Lansing, MI, USA. Her current research interests include electromagnetic, ultrasonic and optical nondestructive testing and evaluation (NDT&E), machine learning algorithms, and computational modeling.

Lalita Udupa received the Ph.D. degree in electrical engineering from Colorado State University, Fort Collins, CO, USA, in 1986.

She is currently a University Distinguished Professor with the Department of Electrical and Computer Engineering, Michigan State University, East Lansing, MI, USA, where she is involved in the nondestructive evaluation (NDE), signal processing, and biomedical applications. Her current research interest includes NDE, such as the development of computational models for electromagnetic NDE, signal and image processing, data fusion, and inverse problem solutions.

Dr. Udupa is a fellow of the American Society of Nondestructive Testing and the Indian Society of Nondestructive Testing.

Satish Udupa (Life Fellow, IEEE) received the Ph.D. degree in electrical engineering from Colorado State University, Fort Collins, CO, USA, in 1983.

He was a Faculty Member with Colorado State University. He was the Whitney Professor of Electrical and Computer Engineering with Iowa State University, Ames, IA, USA. He was the Dean of the College of Engineering and the Chair of the Electrical and Computer Engineering Department, Michigan State University (MSU), East Lansing, MI, USA, where he serves as the Acting President and a University Distinguished Professor. From 1998 to 2003, he was the Permanent Secretary of the World Federation of NDE Centers. He has authored or coauthored extensively. He is the Technical Editor of the *Electromagnetic Nondestructive Testing Handbook* (American Society for Nondestructive Testing). He holds several patents. His current research interests include materials characterization and nondestructive evaluation.

Dr. Udupa is a fellow of the National Academy of Inventors, the Institute of Electrical and Electronics Engineers, the American Society for Nondestructive Testing, the Indian Society for Nondestructive Testing, and the Engineering Society of Detroit. He is also a Full Member of the Academia NDT International. He is a Regional Editor of the *International Journal of Applied Electromagnetics and Mechanics*.

Yiming Deng (Senior Member, IEEE) received the B.S. degree in electrical engineering from Tsinghua University, Beijing, China, in 2003, and the Ph.D. degree in electrical engineering from Michigan State University, East Lansing, MI, USA, in 2009.

He is currently an Associate Professor with the Nondestructive Evaluation Laboratory, Electrical and Computer Engineering Department, College of Engineering, Michigan State University. His current research interests include electromagnetic and acoustic nondestructive evaluation, structural health monitoring for multiscale, multiresolution, and multiparameter damage diagnostics and prognostics, applied electromagnetics, acoustics, and computational modeling.

Dr. Deng is a member of the American Society for Nondestructive Testing (ASNT). He is also an Associate Editor of the *IEEE TRANSACTIONS ON RELIABILITY*, *Materials Evaluation*, and *RAMS Proceedings*. He serves as a Panelist and a Reviewer for the National Science Foundation, the U.S. Department of Energy, the U.S. Department of Transportation, and the NDSEG Program (U.S. DoD and ASEE).